View metadata, citation and similar papers at core.ac.uk

brought to you by CORE

provided by ChesterRep

OPEN ACCESS

IOP Publishing

Nanotechnology

Nanotechnology **32** (2021) 205601 (11pp)

https://doi.org/10.1088/1361-6528/abdf8f

Ice-templated hybrid graphene oxide—graphene nanoplatelet lamellar architectures: tuning mechanical and electrical properties

Pei Yang[1,2], **Gustavo Tontini**[1,*], **Jiacheng Wang**[1,2], **Ian A Kinloch**[1,2] **and Suelen Barg**[1,*]

[1] Henry Royce Institute and Department of Materials, The University of Manchester, Oxford Rd, Manchester, M13 9PL, United Kingdom

[2] National Graphene Institute, The University of Manchester, M13 9PL, United Kingdom

E-mail: Suelen.Barg@manchester.ac.uk and gustavotontini@gmail.com

Received 21 October 2020, revised 12 January 2021

Accepted for publication 25 January 2021

Published 23 February 2021

Abstract

The traditional freeze-casting route for processing graphene-based aerogels is generally restricted to aqueously dispersed flakes of graphene oxide (GO) and post-processing reduction treatments, which brings restrictions to the aerogels electrical properties. In this work, we report a versatile aqueous processing route that uses the ability of GO todisperse graphene nanoplatelets (GNP) to produce rGO-GNP lamellar aerogels via unidirectional freeze-casting. In order to optimise the properties of the aerogel, GO-GNP dispersions were partially reduced by L-ascorbic acid prior to freeze-casting to tune the carbon and oxygen (C/O) ratio. The aerogels were then heat treated after casting to fully reduce the GO. The chemical reduction time was found to control the microstructure of the resulting aeorgels and thus to tune their electrical and mechanical properties. An rGO-GNP lamellar aerogel with density of 20.8 $\pm$ 0.8 mg cm^{-3} reducing using a reduction of 60 min achieved an electrical conductivity of 42.3 S m^{-1}. On the other hand, an optimal reduction time of 35 min led to an aerogel with compressive modulus of 0.51 $\pm$0.06 MPa at a density of 23.2 $\pm$ 0.7 mg cm^{-3}, revealing a compromise between the tuning of electrical and mechanical properties. We show the present processing route can also be easily applied to produce lamellar aerogels on other graphene-based materials such as electrochemically exfoliated graphene.

Supplementary material for this article is available online

Keywords: graphene, graphene aerogel, graphene nanoplatelets, freeze-casting, properties, morphology

(Some figures may appear in colour only in the online journal)

1. Introduction

The outstanding properties of graphene, including its high mechanical strength, high electrical conductivity, low density, and high surface area, grant it potential in a variety of application in composites, nano-electronics, energy storage, sensors, catalyst, and biomedicine [1–3]. A key challenge in

* Authors to whom any correspondence should be addressed.

Original content from this work may be used under the terms of the Creative Commons Attribution 4.0 licence. Any further distribution of this work must maintain attribution to the author(s) and the title of the work, journal citation and DOI.

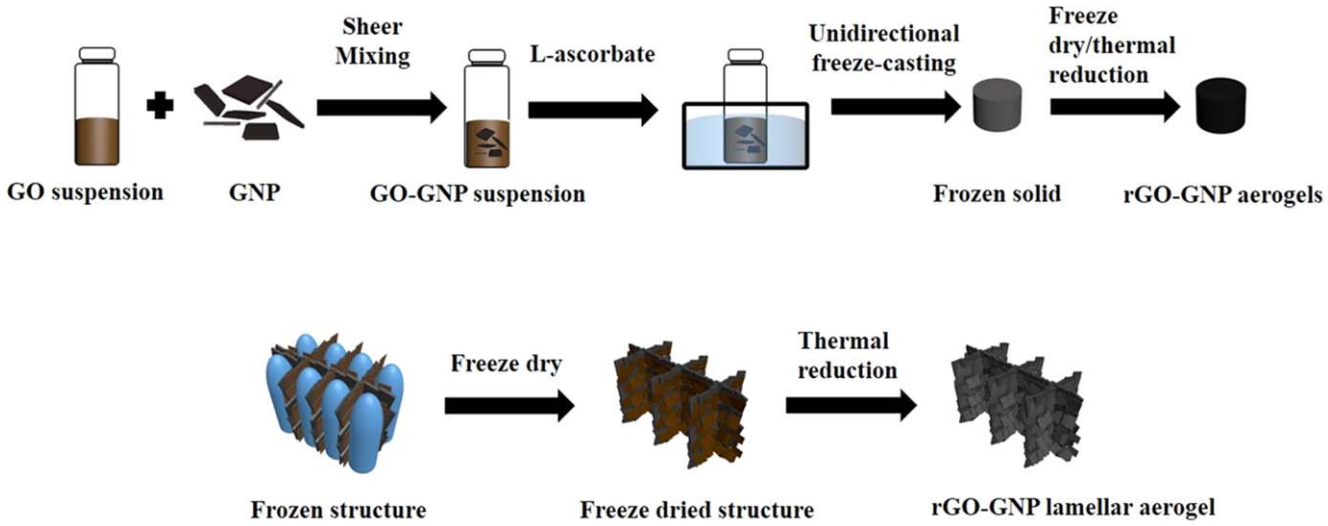

Figure 1. Schematic of the processing route towards rGO-GNP lamellar aerogels. (First row: schematic of processing route for rGO-GNP lamellar aerogels. Second row: Details of processing from fronzen structure to rGO-GNP lamellar aerogel). From left to right: GNP are incorporated into GO aqueous suspensions via shear mixing; the GO-GNP suspensions are partially reduced with L-ascorbic acid at 50 °C for different times *t*; these are subsequently freeze casted and dried to form lamellae structures templated by the ice crystals after a freeze drying step; the aerogels are subjected to a final thermal treatment at 300 °C and 800 °C in Ar.

realizing these applications is translating those promising properties from the nanoscale to bulk materials. One possible solution is the assembly of the 2D materials into aerogels and foams [4–7]. Indeed, graphene-based aerogels have shown excellent properties, such as high electrical conductivity ($\sim$10 S cm^{-1}), thermal resistance and insulation (0.014 W m^{-1}·K^{-1}), and fluid adsorption capacity [4, 8].

Generally, graphene oxide (GO) is the prefered precursor to produce such aerogels due to the aqueous preparation routes used [7, 9–11]. The fabrication of 3D nanoporous structures using GO has been achieved by various methods including freeze-gelation (freeze-casting) [12], chemical reduction [13], and hydrothermal processing [9]. Among all methods, freeze-casting is one of the most popular for obtaining porous 3D structure because it allows the formation of an anisotropic microstructure with controllable and uniform macropores [4, 14]. Water is normally preferable for freeze-casting processing due to its cost effectiveness and environmental friendliness. When Yin *et al.* [15] first assembled a GO 3D structure via freeze-casting method, they have found the produced aerogel to have very promising specific capacitance, around 110 F g^{-1}, confirming its potential in supercapacitor devices. Similarly, Qiu *et al* [16] combined GO with freeze-casting technique to create 3D rGO structures with great elastic properties, being capable of fully recovering from compressive loading even after an 80% compressive strain. More recently, Wang *et al* [17] developed mechanically strong, super elastic rGO aerogel by using bidirectional freeze-casting method. Several parameters, such as flake size, concentration, cooling rate, and mould shape have been found to influence the final microstructure and properties of the formed aerogels [18–20]. Moreover, the GO's carbon to oxygen (C/O) ratio during the freeze-casting can also influence such microstructure [16]. Consequently, despite freeze-casting of GO water suspension being a convenient and scalable method, extra defects are generally introduced to the materials surface, both during processing and post-reduction-treatment, and severely hinder the properties of interest. On the other hand, non-functionalised graphene-based materials, such as pristine graphene and graphene nanoplatelets (GNP), cannot easily be stabilised in suspensions due to their poor dispersability in both aqueous and organic solvents. Several approaches have been studied for the production of stable aqueous suspension of graphene [21–23]. Chemical functionalisation of graphene with highly concentrated acid is a widely used technique to increase the dispersibility [24, 25]. However, the modification via chemical route can disrupt the electronic paths in graphene and deteriorate the electrical and other quantum effect properties of the stuctures [25]. To address this issue, some studies have adopted a non-covalent approach by using surfactant, including charged and uncharged polymers for dispering graphene materials [26, 27], though the stabilizing effect is still limted. Recently, Kazi *et al* [28] has reported that GNP can be dispersed in a GO water suspension over a wide range of pH values. Thus, it would be very useful to combine this approach with freeze casting to create high quality graphene-based aerogels.

In this work, we developed a route of binder-free freeze-cast graphene-based aerogels with tunable C/O ratios (figure 1). The route is based on the use of GO as a multi-purpose colloid that enables the aqueous dispersion of GNP at concentrations as high as 80 wt% (at 4:1 GNP:GO ratios), aids in the formation of the 3D network contribute to the final aerogel properties. The resulting suspension was later processed by unidirectional freeze- casting, freeze-drying, and thermal reduction to obtain a light-weight 3D structure.

Initially we studied the dispersions and role of the chemical reduction time on the oxygen contents of the aerogels, by Raman spectroscopy and x-ray photoelectron spectroscopy. The

GO-GNP suspension stability was characterized via zeta potential before and after the partial chemical reduction process.

2. Materials and methods

2.1. Materials

The reagents used were L-ascorbic acid (Sigma-Aldrich, L-ascorbic acid 99%), graphite flakes (grade 2369, Graphexel Ltd, UK), sodium nitrate (Sigma-Aldrich, ACS reagent ⩾99.0%), potassium permanganate ($KMnO_4$, Sigma-Aldrich, ACS reagent ⩾99.0%), sulfuric acid (ACROS Organics 96% solution in water, extra pure) and hydrogen peroxide (H_2O_2, Scientific Laboratory Supplies, 35% solution in water,). The GNP (M-25, XGScience, USA) had a flake size of 10.7 ± 3.7 μm (figure S1 (available online at stacks.iop.org/NANO/32/205601/mmedia)) and thickness of ∼45 nm (figure S2).

2.2. Synthesis of graphene oxide

GO flakes were produced using a modified Hummers' method [29]. Firstly, 3.8 g of sodium nitrate was dissolved in 169 ml of sulfuric acid and stirred constantly for 10 min in an ice bath. 5 g of graphite flakes was then added and stirred for a further 10 min. Finally, 22.5 g of $KMnO_4$ was gradually added to the mixture over 30 min. The mixture was allowed to warm to room temperature and then continuously stirred for 4 d to consume the $KMnO_4$, as evidenced by the diminished green colour. After the first day, 152 ml sulfuric was added every 24 h for the remaining 3 d. After 4 d, the viscous oxidized mixture was slowly dispersed in a solution of water (983.4 ml), H_2O_2 (8 ml) and sulfuric acid (9 ml) in an ice bath. The mixture became light-yellow and was continuously stirred for 2 h after the initial effervescence stopped. The product was centrifuged at 8000 rpm for 30 min to separate the GO from the acid solution. The GO precipitate was repeatedly washed and centrifuged with the acidic solution (983.4 ml of water, 8 ml of H_2O_2, and 9 ml of sulfuric acid) 7 times, and subsequently washed with deionised water until the pH of the supernatant was about 5 (after 15 washing cycles). The resulting dark brown–orange viscous GO sol (∼10 mg ml^{-1}) was diluted down to 5 mg ml^{-1} using deionised water for further application. The resulting GO had a flake size of 7.8 ± 3.1 μm (figure S1) and thickness of ∼2.6 nm (figure S2).

2.3. Production of the rGO-GNP aerogels

GNP powder was added to 10 ml of the GO suspension (5 mg ml^{-1}) at GNP:GO weight ratios of 4:1 and homogenised in an ice bath (IKA T25 digital Ultra Turrax) at 15 000 rpm for 20 min. A black-coloured aqueous suspension with a solid concentration of 25 mg ml^{-1} GO-GNP was formed. 50 mg of L-ascorbic acid was then added to the suspension (1:1 mass ratio of GO to L-ascorbic acid), homogenised by shear mixing for 10 min in ice bath and then placed into a water bath at 50 °C for a given time, *t* min. Samples were prepared with *t* from 0 to 60 min at 5 min steps to investigate the partial reduction treatment. Then, the partially chemically reduced GO-GNP (denoted as CR*t*) suspension was frozen by unidirectional freeze-casting using a lab-built freeze caster as described in our previous work [30] and a PTFE cylindrical mould (20 mm diameter and 20 mm height). Freeze-casting was conducted from 20 °C to −100 °C at a cooling rate of 5 °C min^{-1}. The frozen samples were freeze-dried to yield aerogels. The as-made CR*t* aerogels did not show any significant electrical conductivity so they were thermally treated at either 300 °C or 800 °C in an argon atmosphere for 40 min.

The resulting samples were labelled as CR*t*TR300 and CR*t*TR800 where '*t*' is the partial chemical reduction (CR) time (min), and TR300, TR800 stand for thermal reduction (TR) at 300 °C and 800 °C, respectively.

2.4. Characterization

The zeta potential of the particles in the GO-GNP suspensions was investigated by a Zetasizer Nano ZS (Malvern Instruments Ltd, Malvern, UK) using 4 mW He–Ne laser operating at a wavelength of 633 nm with detection angle of 13°, the pH of suspension was adjusted by 0.01 mol l^{-1} NaOH buffer solution for higher pH and 0.01 mol l^{-1} HCl buffer solution for lower pH. Raman spectra were collected from the aerogels using a Renishaw System 1000 Raman Spectrometer with a 514 nm excitation laser. X-ray photoelectron spectra (XPS) measurements were performed by a PHI Quantera SXM/AES 650 Auger Electron Spectrometer (ULVAC-PHI, Inc.) equipped with a hemispherical electron analyzer and a scanning monochromated Al K_α ($h\upsilon = 1486.6$ eV) x-ray source. The microstructure of the aerogels was investigated by using scanning electron microscopy (FEI, Quanta 250). The density of the aerogels was determined by measuring their dimensions using a digital Vernier calliper and their mass using a balance with 0.001 mg accuracy. The mechanical properties of the aerogels was measured using an Instron 3344L3927 in compression mode with load speed of 0.5 mm s^{-1} and unload speed of 0.05 mm s^{-1} due to the slow recovery rate. The electrical impedance was measured by NumetriQ PSM1735 analyzer where the samples were coated with silver paint on both sides in order to reduce the contact resistance.

3. Results and discussion

3.1. Rheology of suspension as a function of chemical reduction time

The as-prepared GO-GNP suspensions were found to go from an initial liquid behaviour to gel behaviour during the 60 min reduction with an excess of L-ascorbic acid (figure 2). Cone and plate rheology found that the viscosity went from 0.17 Pa·s to 4.7 Pa·s after 35 min reduction (CR35), and 10.2 Pa·s after 60 min (CR60) (figure 3(a)). This gelation was due to the enhanced π–π interactions between the GO flakes after partial chemical reduction and the reduced hydrophlilc nature to prevent dispersion but left enough for hydrogen briding which caused the formation of a weekly cross-linked network

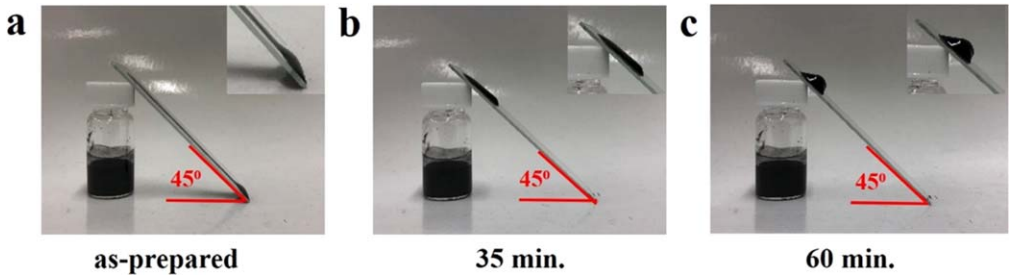

Figure 2. Digital images of GO-GNP suspensions as-prepared CR0 (a); after 35 min CR35 (b); and after 60 min CR60 (c) of chemical reaction. Insets show magnified digital image of a droplet of the respective suspension on a 45° inclined glass slide after 60 min.

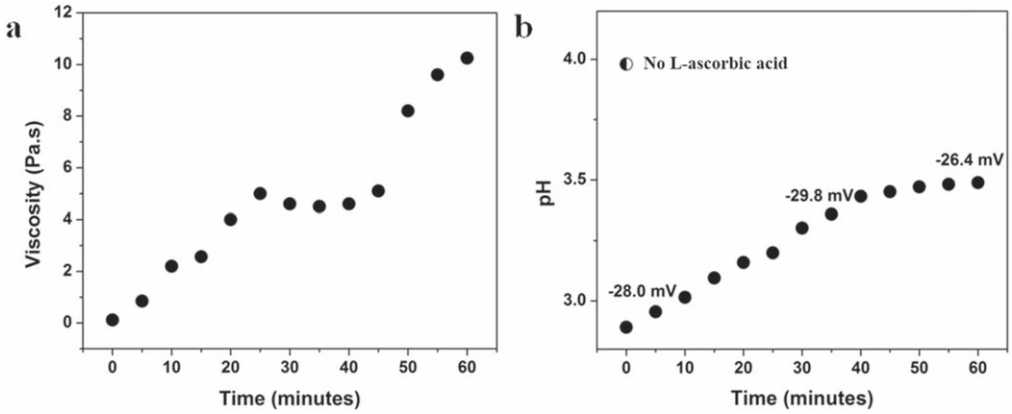

Figure 3. (a) Viscosity (shear rate at 1 S^{-1}) and (b) as-measure pH value of GO-GNP suspensions for different chemical reduction time (at 50 °C). The pH value of a suspension upon the addition of with no chemical reduction step is indicated with the half-filled symbol in (b). The corresponding zeta potential values of GO-GNP suspensions at 5, 35, and 60 min of reaction is indicated in (b).

within the suspension [31, 32] (figures 2 and 3). The pH was monitored as a function of time upon the addition of acid to monitor the reduction of the GO. The initial pH value of the suspension was 3.9 (figure 3(b)) and it dropped to 2.8 immediately upon the L-ascorbic acid addition. After 40 min the graphene oxide appeared to be fully reduced and no further pH changes were observed. De Silva *et al.* suggested that the functional groups such as carbonyl and carboxylate groups on GO are gradually removed whilst consuming the $H^{+}_{(aq)}$, leading to a the rise of the pH to 3.5 with reduction time [33].

The Zeta potential of the suspension was measured to further understand the suspension's behaviour. It was found CR5, CR35 and CR60 was -28 ± 2 mV. However, the Zeta potential has a complex dependence on both the pH and degree of reduction. It is important, though in controlling the formation of the hydrogel, hence these factors was explored in more details. The as-made GO, GNP and the GO-GNP dispersions were studied as a function of pH between 2 and 4 using a 0.01 mol l^{-1} buffer solution. As can be seen in figure 3(b), the studied suspensions after chemical reduction (from 0 to 60 min) present pH in the investigated range. At all pHs, the GO had a considerable lower value and broader distribution of the Zeta potential than GNP in accordance to Salim *et al*'s report. [34] This difference is due to their oxygen functional groups (hydroxyl, carboxyl, and carbonyl), which gives high density of electrical charge per unit area (figure 4).

The GO-GNP suspensions show a single peak that goes from around −17.5 mV for pH 2 to −35.3 mV for pH 4, indicating a stable colloidal suspension specially for pH above 2 [35]. The lack of a bi-modal distribution is an evidence that the GO and GNP have aggregated with each other [28]. GNP have a relatively defect-free basal plane which is hydrophobic in nature with a low surface charge measured between −1.2 and −2.7 mV [35, 36]. However, in the presence of GO sheets, GNP flakes can attach to them via van der Waals and repulsive electrostatic forces [34–36] leading to GO-GNP hybrid flakes with a zeta potential closer to that of GO, making it stable in water.

3.2. Production of areogels

The CR*t* suspensions were unidirectionally freeze-cast and freeze-dried to form free-standing aerogels with both cilindrical (diameter = 2 cm) and rectangular (8 cm × 2 cm × 0.8 cm) shapes as shown in figure 5. The CR0 samples show a density of $\sim 33.2 \pm 2.1$ mg cm^{-3}, and after chemical and thermal treatment, the CR*t*TR300 samples show lower densities between ∼21 and ∼28 g cm^{-3} (table 1). The lower density for CR*t*TR300 samples is due to removal of functional groups from GO surfaces and a lower volume shrinkage

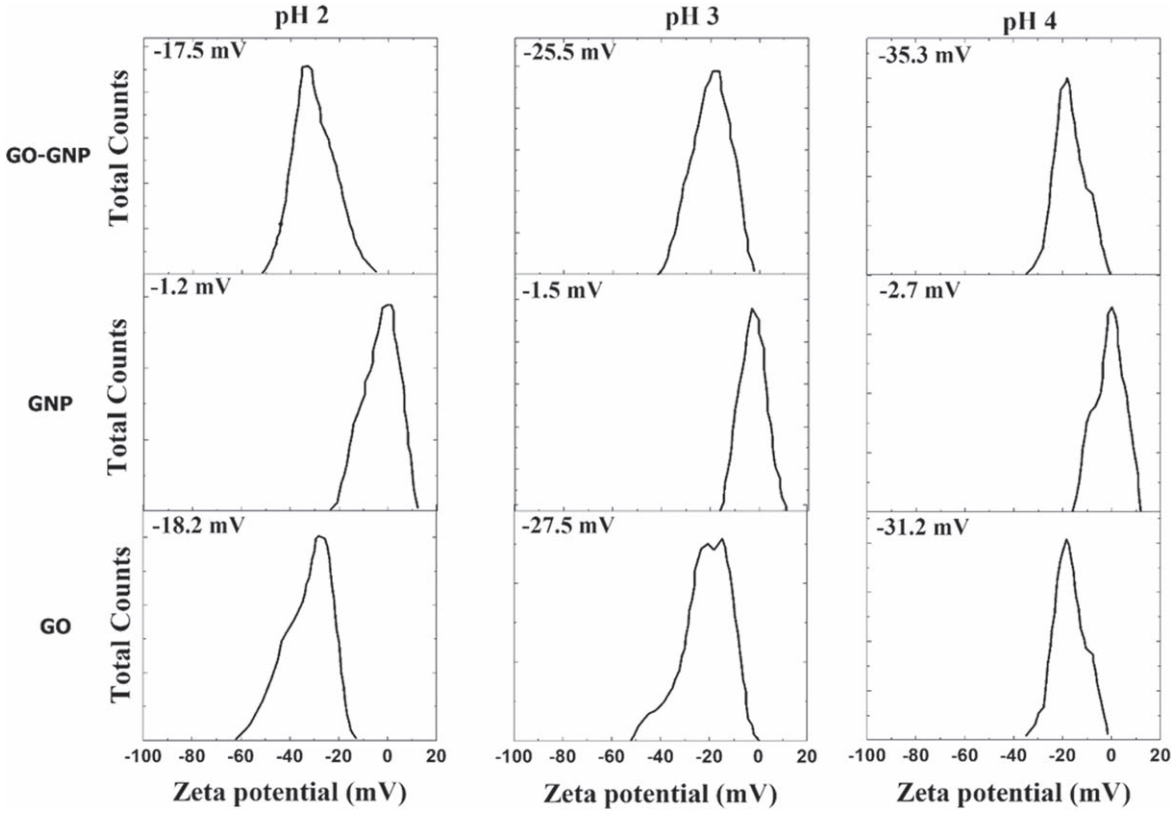

Figure 4. Zeta potential distribution for as made of GO-GNP, GNP, and GO suspensions as function of the buffer solution pH.

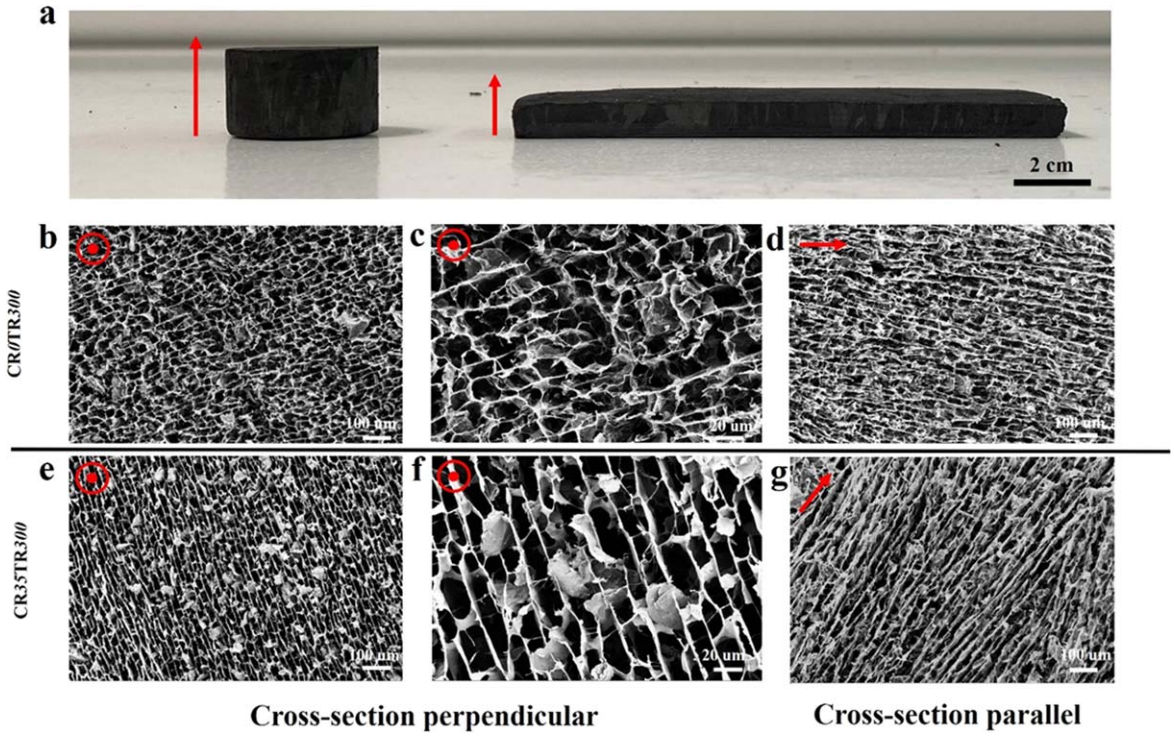

Figure 5. (a) Photograph of different shape CR*f*TR300 aerogels produced by the developed route. (b) SEM images of the cross-section perpendicular to the freezing direction of CR*0*TR300; (c) the cross-sections perpendicular to the freezing direction with higher magnification, (d) cross-section parallel to the freezing direction. (e) SEM images of the cross-section perpendicular to the freezing direction of CR35TR300, (f) the cross-section perpendicular to the freezing direction with higher magnification; (g) cross-section parallel to the freezing direction. Red circles and arrows in the images indicate the freezing direction.

Table 1. Summary of processing parameters, samples density and samples volume shrinkage (before and after freeze dry) for all produced samples and XPS spectroscopy result of oxygen content and carbon/oxygen content ratio for CR0, CR5TR300, CR35TR300, CR60TR300 and CR60TR800 aerogels.

Sample	Chemical reduction time (min)	Thermal reduction temperature (°C)	Thermal reduction time (min)	Density (mg cm^{-3})	Oxygen content (at%)	C/O ratio	Sample volume shrinkage
CR0	0	0	0	33.2 ± 2.1	40.1	4.2	9.7%
CR0TR300	0	300	40	31.3 ± 1.1	8.5	10.8	6.5%
CR5TR300	5	300	40	27.9 ± 0.7			5.9%
CR10TR300	10	300	40	27.3 ± 0.6			5.3%
CR15TR300	15	300	40	27.4 ± 1.2			5.7%
CR20TR300	20	300	40	25.3 ± 0.9			5.2%
CR25TR300	25	300	40	25.6 ± 0.4			6.4%
CR30TR300	30	300	40	22.4 ± 1.3			5.6%
CR35TR300	35	300	40	23.2 ± 0.7	6.6	14.2	5.9%
CR40TR300	40	300	40	24.3 ± 1.3			4.3%
CR45TR300	45	300	40	22.4 ± 0.5			6.3%
CR50TR300	50	300	40	23.6 ± 0.7			5.9%
CR55TR300	55	300	40	22.1 ± 0.9			5.5%
CR60TR300	60	300	40	22.3 ± 0.6	5.7	15.8	5.7%
CR60TR800	60	800	40	20.8 ± 0.8	3.2	30.3	7.2%

due to stronger bonding formed by the partial chemical reduction [37].

The internal structure of the network consisted of long microscopic channels oriented parallel to the ice growth direction and separated by thin walls that were formed by the rearrangement of GO and GNP flakes between ice crystals during freezing (figure 5). Althought the weight ratio of GNP is much higher than GO (4:1), due to the large specific area from the oxide thin flakes, the aerogels scaffold is mainly formed by GO while thick GNP flakes are found amidst the network (figures 5(c), (f)). The aerogels produced from the suspensions that undergo a partial reduction step of 35 min (figures 5(e)–(g)—CR35TR300) resulted in the formation of more defined elongated lamellar pores that extend across larger domain areas as compared to CR0TR300 samples (figures 5(b)–(d)). Form the cross-sectional SEM images of the aerogels produced with figure 5(b) and without figure 5(e) partial reduction step, it can be see that chemical reduction helps in the formation of more defined lamellar channels and extend across larger areas. The freeze-casting process is governed by complex and dynamic liquid-particle and particle-particle interactions. Other studies have previously reported that the oxygen content is one of the factors that can affect these interactions [16]. The degree of reduction of the GO colloids prior to freezing, controls the surface characteristics of the flake [31], which in turn can influence the flake-flake interactions, promoting the network formation and/or their rejection from the freezing front [16]. During freeze-casting, as the ice crystals grow anisotropically, both GO and partially reduced GO suspensions can stabilize the GNP in water, allowing the freeze-casting technique to create homogeneous porous networks. As partially reduced GO sheets are less hydrophilic and more rejected than non-reduced GO, those are forced to align along the moving solidification front, concentrating and squeezing at the crystal boundaries and yielding a highly ordered layered assembly [16, 38]. As a result, a more anisortropic structure can be obtained when some partial chemical reduction is employed prior to processing. However, longer chemical reduction periods, leads to the suspensions to becomimg too thick (figures 2 and 3), hindering the mobility of the solid phase within the suspension during freezing and strongly influencing on the final microstructure of the aerogels [16, 39] (figure S3).

Raman spectra of rGO region of final aerogels are shown in figure 6(a). The as-prepared GO exhibits typical features from graphene oxide materials, for example, the G band (∼1580 cm^{-1}) has a similar intensity of the D band (∼1350 cm^{-1}) ($I_D/I_G \sim 1$) [40]. The D band signature is associated with structural defects and the partially disordered structure of graphitic domains. The intensity ratio I_D/I_G decreases from ∼0.89 for CR0TR300 to ∼0.62 for CR35TR300 and ∼0.41 for CR60TR300. The figure 6(b) shows how the I_D/I_G ratio varies as function of partial chemical reduction time. It can be observed that the L-ascorbic acid has a significant effect on removing functional groups, reorganizing the structure of GO-GNP aerogels and leading to a decrease on the ratio between D and G band intensities. However, as pointed out previously, a too long chemical reduction time will increases the viscosity even further, starting to transform the suspension into a gel (figures 2 and 3), and significantly restricts the solid phase mobility, reducing the anisotropy (sample CR60TR300 (figure S3)).

XPS spectroscopy was also employed to investigate chemical structure and composition of the as-prepared GO, GNP, and the aerogel samples. The C/O atomic ratios have increased from 1.5 for GO to 4.2 for the CR0 mixture (table S1) due to the additional GNP. All treated samples show a considerable decrease of the intensity for O 1s binding energies around 530.8 eV indicating successful reduction of the GO (figure 6(c)). After a thermal treatment, the sample

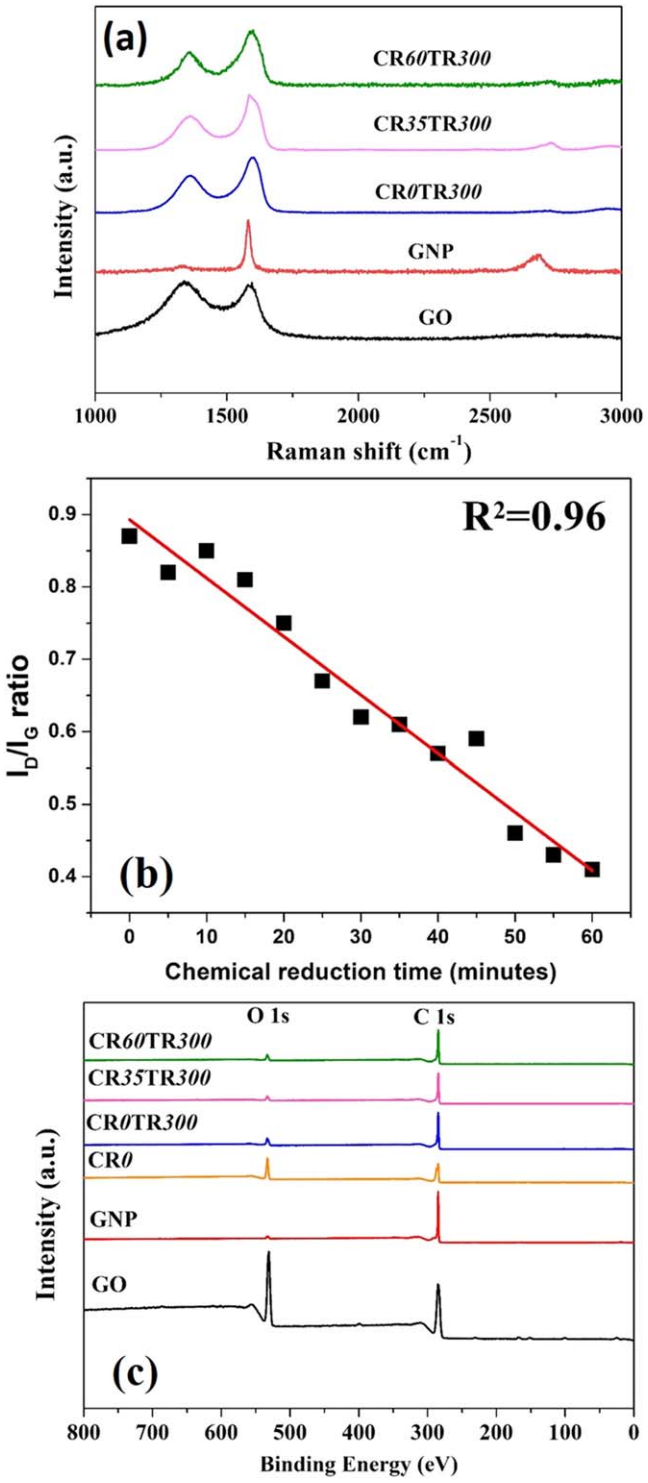

Figure 6. (a) Raman spectroscopy patterns for CR*f*TR300 aerogels with rGO region (CR0TR300, CR35TR300 and CR60TR300 aerogels) and starting GO and GNP (b) Raman spectroscopy I_D/I_G ratio (Intensity ratio of D band and G band from Raman spectroscopy) for CR*f*TR300 aerogels with rGO region as a function of partial chemical reduction time; (c) XPS spectroscopy measurements were undertaken on CR0 and CR*f*TR300 aerogel samples (CR0TR300, CR35TR300 and CR60TR300 aerogels), starting GO and GNP.

CR0TR300 presented a C/O atomic ratio of 10.8. Meanwhile, the C/O ratio of the samples that underwent a pre-partial chemical reduction, CR35TR300 and CR60TR300,

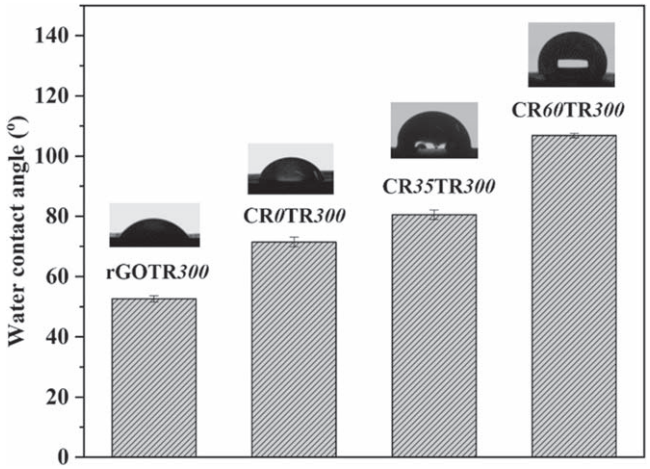

Figure 7. Water contact angles for rGO (rGOTR300) and rGO-GNP aerogels (CR0TR300, CR35TR300 and CR60TR300).

increased to 14.2 and 15.8, respectively. Figure S4 in the support information shows an extract of the XPS region of C 1s binding energies (280–298 eV) where it is also possible to see the decrease of oxygen-containing groups with the increase of chemical reduction time.

Another property of interest of aerogels is their wettability. For example, hydrophobic graphene-based aerogels have shown promising potential as efficient oil absorbent, self-cleaning, and anti-icing materials [41]. However, due to the hydrophilic nature of GO, GO-based aerogels generally show a relatively high hydrophilicity, demanding further high temperature thermal reduction processes to tune this property. Alternatively, figure 7 shows that the addition of GNP resulted in the increase of WCA value from 50.6° for pure rGO to 70.2° for rGO-GNP (both treated at only 300 °C) due to the hydrophobic nature of the GNP. As the treatment time for the chemical reduction is increased, the WCA increased and reached 106.8° for CR60TR300, being the highest among all the samples. This increase in hydrophobicity of the aerogels is mainly due to the reduction in oxygen containing functional groups on GO as the result of chemical and thermal reduction, as indicated by the XPS and the Raman results.

The compressive stress–strain curves in figure 8(a) can be divided into three parts: linear elastic, yielding, and recovery parts. Sample CR35TR300 reaches its yielding region at around 7% compressive strain which is much ealier compared to the 15% with in both samples CR60TR300 and CR0TR300. Futerhmore, the samples CR35TR300 and CR60TR300 show improved recoverability after experiencing large strains compared to the non-chemically treated sample CR0TR300 (figure 8(a)). The compressive modulus of CR*f*TR300 samples (figure 8(b)) were calculated from the stress–strain curves (figure 8(a)). The results show the compressive modulus improves as the chemical reduction time of suspensions increases up to an optimum at 35 min (CR35TR300 samples). However, as the chemical treatment time increased, the compressive modulus decreases down to to 0.06 ± 0.009 MPa for 60 min reduction time (samples CR60TR300). It is mostly accepted that the compressive

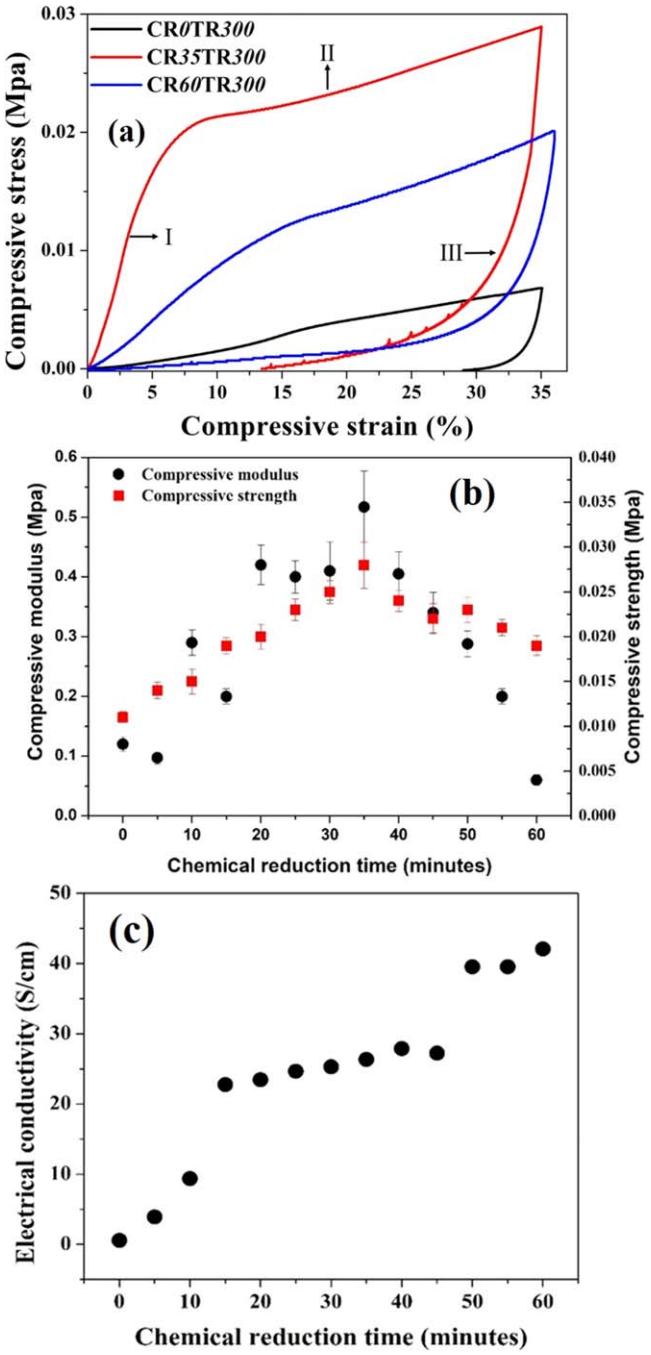

Figure 8. (a) Compressive stress–strain curves of CR*t*TR300 aerogels (I: linear elastic region, II: yielding region and III: recovery region). (b) Compressive modulus and strength of CR*t*TR300 aerogels for different chemical reduction times. (c) Electrical conductivities of CR*t*TR*300* aerogels for different chemical reduction times.

properties and behaviour of graphene aerogel are directly related to its density [42, 43], however, as can be seen, a significant difference of compressive modules is found on samples with very similar density. The high compressive strength of CR35TR300 is due to its more organized lamellar hierarchical structure compared to CR60TR300 which has more disordered structures and relatively smaller pores (as can be seen in figures 5(e)–(g) and S3). This kind of lamellar structure usually results in high elasticity and mechanical robustness [43, 44]. In order to elucidate the effect of the chemical reduction on the properties of the aerogels, we compared sample CR35TR300 with CR0TR300 (no chemical reduction). Although ordered structures have been obtained within aerogels with no chemical reduction, their mechanical and electrical properties (figures 8(b) and (c)) are lower as compared to the chemically reduced samples. The chemical reduction step can contribute to the formation of a stronger network of partially reduced flakes before the freeze-casting step [45]. It has also shown to contribute to the restoring of the sp^2 network and reducing the amount of defects on GO flake [46]. Consequently, besides the ordered lamellar architectures these effects can also contribute to the properties of the aerogels.

The conductivity of rGO-GNP aerogels has increased from 0.65 S m^{-1} with no chemical reduction(CR0TR300, I_D/I_G ratio of 0.89) to 42.3 S m^{-1} after 60 minutes reduction (CR60TR300, I_D/I_G ratio of 0.41). This behaviour can be attributed to the restoration of sp^2 carbon network facilitating the electrons transfer within the network [47].

For graphene aerogels, several studies show that the electrical conductivity can be related to the thermal reduction temperature and bulk density [47–49]. Figure 9 shows a comparison between the electrical conductivity and compressive modulus obtained for the aerogels developed in this work and data from literature (values are also summarized in table S2 and table S3). One can observe that rGO-GNP samples show a tunable mechanical and electrical properties without changing the density. Furthermore, additional tests were made by increasing the thermal reduction temperature to 800 °C, increasing GNP:GO ratio, and using electorchemical exfoliated graphene (EEG) instead of GNP (figure S5). It is observed that the electrical conductivity of samples increased to 77.4 S m^{-1} when higher thermal reduction was employed. Increasing the GNP content (GNP:GO mass ratio of 1:8) in the samples considerably increases their density (~38.4 mg cm^{-3}) and electrical conductivity (114.7 S m^{-1}). Finally, GO was also shown to be able to disperse other poor dispersibility graphene-based materials such as EEG. Following the same protocol presented in this work rGO-EEG aerogels were produced, showing greater electrical conductivity (131.8 S m^{-1}) with ~36.8 mg cm^{-3} density, as can be seen in the supplementary info (figure S5).

4. Conclusion

In this work, we developed a simple and scalable route to fabricate rGO-GNP hybrid lamellar architectures by combining partial chemical reduction and unidirectional freeze-casting followed by a final heat treatment step. GO was shown to effectively stabilise GNP in aqueous dispersions, allowing controlled freeze-casting of the hybrid system. The partial chemical reduction was used to control flow properties and flake-flake interactions and the freeze-casting process created the highly anisotropic structures. The partial chemical reduction time is shown to impact both the electrical and

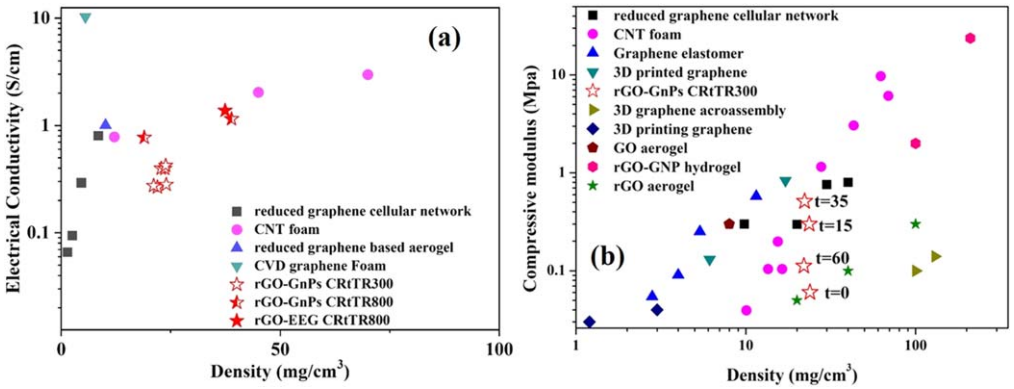

Figure 9. Electrical conductivity of CR*t*TR300 (with *t* min chemical reduction and 300 °C thermal reduction for 40 min at Ar atmosphere), CR*t*TR800 (with *t* min chemical reduction and 800 °C thermal reduction for 40 min at Ar atmosphere) and rGO-EEG CR*t*TR800 (GO with electrically exfoliated graphene at *t* min chemical reduction and 800 °C thermal reduction for 40 min at Ar atmosphere) (a) and compressive modulus of CR*t*TR300 samples (with *t* min chemical reduction and 300 °C thermal reduction for 40 min at Ar atmosphere) developed in this work in comparison to literature values for other nanocarbon-based materials. Reduced-graphene cellular network [47], CNT foam [50], reduced graphene based aerogel [51], CVD graphene foam [52], graphene elastomer [16], 3D printed graphene [53], 3D graphene acroassembly [51], 3D printing graphene [48], GO aerogel [17], rGO-GNP hydrogel [54] and rGO aerogel [16, 19, 44, 55].

mechanical properties of the aerogels obtained. The CR35TR300 samples (chemical reduced for 35 min) exhibited the highest compressive modulus (0.51 ± 0.06 Mpa and strength of 0.028 ± 0.0026 Mpa) amongst all the samples with great recoverability after a large strain of 35%. By adjusting the processing and formulation parameters, the aerogels microstructure, C/O ratio, and properties can be fine tuned for a wide range of applications. The protocol reported in this work can also be applied to other graphene-based materials. Electrochemical exfoliated graphene was also used as a proof-of-concept to demonstrate the practical opportunities in the development of lightweight graphene-based lamellar architectures for functional and structural applications.

Acknowledgments

JW and SB acknowledge financial support from Heilongjiang Huasheng Graphite Co., People's Republic of China. GT acknowledges financial support from the Coordenação de Aperfeiçoamento de Pessoal de Nível Superior, Brasil (CAPES). IAK acknowledges Morgan Advanced Materials and RAEng for funding his Chair.

Data availability statement

All data that support the findings of this study are included within the article (and any supplementary files).

Author contributions

PY synthesised and processed all samples, conducted the general characterization, electrical conductivity test and mechanical test. JW conducted the Raman spectroscopy. PY, and GT* wrote and proofread the manuscript and all author contributed to analysis and interpretation of the results. SB* and IAK supervised the research. All authors have given approval to the final version of the manuscript. *Corresponding authors.

Note

The authors declare no conflicts of interest.

ORCID iDs

Pei Yang https://orcid.org/0000-0002-4639-2076
Gustavo Tontini https://orcid.org/0000-0002-2453-6358
Jiacheng Wang https://orcid.org/0000-0001-7301-3310
Ian A Kinloch https://orcid.org/0000-0003-3314-6869
Suelen Barg https://orcid.org/0000-0002-0723-7081

References

[1] Olabi A G, Abdelkareem M A, Wilberforce T and Sayed E T 2021 Application of graphene in energy storage device—a review *Renew. Sustain. Energy Rev.* **135** 1364-0321
[2] Kumar A, Sharma K and Dixit A R 2019 A review of the mechanical and thermal properties of graphene and its hybrid polymer nanocomposites for structural applications *J. Mater. Sci.* **54** 5992-6026
[3] Dasari Shareena T P, McShan D, Dasmahapatra A K and Tchounwou P B 2018 A review on graphene-based nanomaterials in biomedical applications and risks in environment and health *Nano-Micro Lett.* **10** 53
[4] Gorgolis G and Galiotis C 2017 Graphene aerogels: a review *2D Mater.* **4** 032001
[5] Tontini G, Greaves M, Ghosh S, Bayram V and Barg S 2020 MXene-Based 3D porous macrostructures for electrochemical energy storage *J. Phys. Mater.* **3** 022001

[6] Kim J E, Oh J H, Kotal M, Koratkar N and Oh I K 2017 Self-assembly and morphological control of three-dimensional macroporous architectures built of two-dimensional materials *Nano Today* **14** 100–23

[7] Wu Y, Zhu J and Huang L 2019 A review of three-dimensional graphene-based materials: synthesis and applications to energy conversion/storage and environment *Carbon* **143** 610–40

[8] Gorgolis G and Karamanis D 2016 Solar energy materials for glazing technologies *Sol. Energy Mater. Sol. Cells* **144** 559–78

[9] Yuxi X, Kaixuan Sheng C L and Shi G 2010 Self-assembled graphene hydrogel *ACS Nano* **4** 4324–30

[10] Qian Y, Ismail I M and Stein A 2014 Ultralight, high-surface-area, multifunctional graphene-based aerogels from self-assembly of graphene oxide and resol *Carbon* **68** 221–31

[11] Wang J, Liu Y, Fan Z, Wang W, Wang B and Guo Z 2019 Ink-based 3D printing technologies for graphene-based materials: a review *Adv. Compos. Hybrid Mater.* **2** 1–33

[12] Wang C, Chen X, Wang B, Huang M, Wang B, Jiang Y and Ruoff R S 2018 Freeze-casting produces a graphene oxide aerogel with a radial and centrosymmetric structure *ACS Nano* **12** 5816–25

[13] Li J, Meng H, Xie S, Zhang B, Li J, Li L, Ma H, Zhang J and Yu M 2014 Ultra-light, compressible and fire-resistant graphene aerogel as a highly efficient and recyclable absorbent for organic liquids *J. Mater. Chem.* A **2** 2934–41

[14] Shao G, Hanaor D A H, Shen X and Gurlo A 2020 Freeze casting: from low-dimensional building blocks to aligned porous structures—A review of novel materials, methods, and applications *Adv. Mater.* **32** 1907176

[15] Yin S, Niu Z and Chen X 2012 Assembly of graphene sheets into 3D macroscopic structures *Small* **8** 2458–63

[16] Qiu L, Liu J Z, Chang S L Y, Wu Y and Li D 2012 Biomimetic superelastic graphene-based cellular monoliths *Nat. Commun.* **3** 1–7

[17] Wang C, Chen X, Wang B, Huang M, Wang B, Jiang Y and Ruo R S 2018 Freeze-Casting Produces a Graphene Oxide Aerogel with a Radial and Centrosymmetric Structure *ACS Nano* **12** 5816–25

[18] Scotti K L and Dunand D C 2018 Freeze casting—a review of processing, microstructure and properties via the open data repository, FreezeCasting.net *Prog. Mater. Sci.* **94** 243–305

[19] Gao W, Zhao N, Yao W, Xu Z, Bai H and Gao C 2017 Effect of flake size on the mechanical properties of graphene aerogels prepared by freeze casting *RSC Adv.* **7** 33600

[20] Zhu X *et al* 2020 Precise control of versatile microstructure and properties of graphene aerogel: Via freezing manipulation *Nanoscale* **12** 4882–94

[21] Gurunathan S, Han J W, Eppakayala V, Dayem A A, Kwon D N and Kim J H 2013 Biocompatibility effects of biologically synthesized graphene in primary mouse embryonic fibroblast cells *Nanoscale Res. Lett.* **8** 393

[22] Wang F, Han L, Zhang Z, Fang X, Shi J and Ma W 2012 Surfactant-free ionic liquid-based nanofluids with remarkable thermal conductivity enhancement at very low loading of graphene *Nanoscale Res. Lett.* **7** 314

[23] Xie H, Yu W, Li Y and Chen L 2011 Discussion on the thermal conductivity enhancement of nanofluids *Nanoscale Res. Lett.* **6** 124

[24] Baby T T and Ramaprabhu S 2011 Enhanced convective heat transfer using graphene dispersed nanofluids *Nanoscale Res. Lett.* **6** 289

[25] Mu X, Wu X, Zhang T, Go D B and Luo T 2014 Thermal transport in graphene oxide—from ballistic extreme to amorphous limit *Sci. Rep.* **4** 3909

[26] Noh Y J, Joh H I, Yu J, Hwang S H, Lee S, Lee C H, Kim S Y and Youn J R 2015 Ultra-high dispersion of graphene in polymer composite via solvent free fabrication and functionalization *Sci. Rep.* **5** 9141

[27] Yuan B, Sun Y, Chen X, Shi Y, Dai H and He S 2018 Poorly-/well-dispersed graphene: Abnormal influence on flammability and fire behavior of intumescent flame retardant *Composites* A **109** 345–54

[28] Kazi S N, Badarudin A, Zubir M N M, Ming H N, Misran M, Sadeghinezhad E, Mehrali M and Syuhada N I 2015 Investigation on the use of graphene oxide as novel surfactant to stabilize weakly charged graphene nanoplatelets *Nanoscale Res. Lett.* **10** 212

[29] Hirata M, Gotou T, Horiuchi S, Fujiwara M and Ohba M 2004 Thin-film particles of graphite oxide 1:: High-yield synthesis and flexibility of the particles *Carbon* **42** 2929–37

[30] Bayram V *et al* 2020 MXene tunable lamellae architectures for supercapacitor electrodes *ACS Appl. Energy Mater.* **3** 411–22

[31] Yang H, Zhang T, Jiang M, Duan Y and Zhang J 2015 Ambient pressure dried graphene aerogels with superelasticity and multifunctionality *J. Mater. Chem.* A **3** 19268–72

[32] Shenoy S L, Painter P C and Coleman M M 1999 The swelling and collapse of hydrogen bonded polymer gels *Polymer* **40** 4853–63

[33] De Silva K K H, Huang H H, Joshi R K and Yoshimura M 2017 Chemical reduction of graphene oxide using green reductants *Carbon* **119** 190–9

[34] Kazi S N, Badarudin A, Zubir M N M, Ming H N, Misran M, Sadeghinezhad E, Mehrali M and Syuhada N I 2015 Investigation on the use of graphene oxide as novel surfactant to stabilize weakly charged graphene nanoplatelets *Nanoscale Res. Lett.* **10** 212

[35] Lu J, Do I, Fukushima H, Lee I and Drzal L T 2010 Stable aqueous suspension and self-assembly of graphite nanoplatelets coated with various polyelectrolytes *J. Nanomater.* **2010** 186486

[36] Wolf E L 2014 Practical Productions of Graphene, Supply and Cost *Applications of Graphene* (*Springer Briefs in Materials*) (Cham: Springer) pp 19–38

[37] Karamikamkar S, Abidli A, Behzadfar E, Rezaei S, Naguib H E and Park C B 2019 The effect of graphene-nanoplatelets on gelation and structural integrity of a polyvinyltrimethoxysilane-based aerogel *RSC Adv.* **9** 11503–20

[38] Kotal M, Kim J, Oh J and Oh I K 2016 Recent progress in multifunctional graphene aerogels *Front. Mater.* **3** 1–22

[39] Deville S and Ice-templating I B O F 2017 Ice-templating, freeze casting: beyond materials processing *Journal of Materials Research* **28** 2202–19

[40] Vallés C, Beckert F, Burk L, Mülhaupt R, Young R J and Kinloch I A 2016 Effect of the C/O ratio in graphene oxide materials on the reinforcement of epoxy-based nanocomposites *J. Polym. Sci.* B **54** 281–91

[41] Mi H Y, Jing X, Huang H X, Peng X F and Turng L S 2018 Superhydrophobic Graphene/Cellulose/Silica aerogel with hierarchical structure as superabsorbers for high efficiency selective oil absorption and recovery *Ind. Eng. Chem. Res.* **57** 1745–55

[42] Patil S P, Shendye P and Markert B 2020 Molecular investigation of mechanical properties and fracture behavior of graphene aerogel *J. Phys. Chem.* B **124** 6132–9

[43] Qin Z, Jung G S, Kang M J and Buehler M J 2017 The mechanics and design of a lightweight three-dimensional graphene assembly *Sci. Adv.* **3** 2375–548

[44] Ni N, Barg S, Garcia-Tunon E, MacUl Perez F, Miranda M, Lu C, Mattevi C and Saiz E 2015 Understanding mechanical response of elastomeric graphene networks *Sci. Rep.* **5** 1–14

[45] Xu Y, Sheng K, Li C and Shi G 2010 Self-assembled graphene hydrogel via a one-step hydrothermal process *ACS Nano* **4** 4324–30

[46] Ni N, Barg S, Garcia-Tunon E, MacUl Perez F, Miranda M, Lu C, Mattevi C and Saiz E 2015 Understanding mechanical response of elastomeric graphene networks *Sci. Rep.* **5** 13712

[47] Barg S, Perez F M, Ni N, Do Vale Pereira P, Maher R C, Garcia-Tuñon E, Eslava S, Agnoli S, Mattevi C and Saiz E 2014 Mesoscale assembly of chemically modified graphene into complex cellular networks *Nat. Commun.* **5** 4328

[48] Zhang Q, Zhang F, Medarametla S P, Li H, Zhou C and Lin D 2016 3D printing of graphene aerogels *Small* **12** 1702–8

[49] Cheng Y, Zhou S, Hu P, Zhao G, Li Y, Zhang X and Han W 2017 Enhanced mechanical, thermal, and electric properties of graphene aerogels via supercritical ethanol drying and high-Temperature thermal reduction *Sci. Rep.* **7** 1439

[50] Worsley M A, Kucheyev S O, Satcher J H, Hamza A V and Baumann T F 2009 Mechanically robust and electrically conductive carbon nanotube foams *Appl. Phys. Lett.* **94** 073115

[51] Worsley M A *et al* 2012 Mechanically robust 3D graphene macroassembly with high surface area *Chem. Commun.* **48** 8428–30

[52] Chen Z, Ren W, Gao L, Liu B, Pei S and Cheng H M 2011 Three-dimensional flexible and conductive interconnected graphene networks grown by chemical vapour deposition *Nat. Mater.* **10** 424–8

[53] García-Tuñon E, Barg S, Franco J, Bell R, Eslava S, D'Elia E, Maher R C, Guitian F and Saiz E 2015 Printing in three dimensions with Graphene *Adv. Mater.* **27** 1688–93

[54] Yang J, Li X, Han S, Zhang Y, Min P, Koratkar N and Yu Z Z 2016 Air-dried, high-density graphene hybrid aerogels for phase change composites with exceptional thermal conductivity and shape stability *J. Mater. Chem.* A **4** 18067–74

[55] Liu X, Pang K, Yang H and Guo X 2020 Intrinsically microstructured graphene aerogel exhibiting excellent mechanical performance and super-high adsorption capacity *Carbon* **161** 146–52